SEDIMENTOLOGY the journal of the International Association of Sedimentologists

Sedimentology (2021) **68**, 1091–1108 doi: 10.1111/sed.12818

The role of sediment gravity flows on the morphological development of a large submarine canyon (Taiwan Canyon), north-east South China Sea

WEI LI*,†,‡,§, SHUANG LI*,†,‡,§, TIAGO M. ALVES¶, MICHELE REBESCO** and YINGCI FENG*,†,‡

**CAS Key Laboratory of Ocean and Marginal Sea Geology, South China Sea Institute of Oceanology, Chinese Academy of Sciences, Guangzhou, 510301, China (E-mail: wli@scsio.ac.cn)*

†Southern Marine Science and Engineering Guangdong Laboratory, Guangzhou, 511458, China

‡Innovation Academy of South China Sea Ecology and Environmental Engineering, Chinese Academy of Sciences, Guangzhou, 510301, China

§University of Chinese Academy of Sciences, Beijing, 100049, China

¶3D Seismic Lab, School of Earth and Ocean Sciences, Cardiff University, Main Building, Park Place, Cardiff, CF10 3AT, UK

***Istituto Nazionale di Oceanografia e di Geofisica Sperimentale (OGS), Borgo Grotta Gigante 42/C, Trieste, 34010, Italy*

Associate Editor – Zhifei Liu

ABSTRACT

High-resolution multibeam bathymetric and multichannel seismic data are used to investigate the morphology of a submarine canyon (Taiwan Canyon), and its surrounding strata, in the north-east South China Sea. This submarine canyon shows two main branches at its head, and changes its orientation from north-west/south-east to east–west due to the effect of a tectonically active seamount. The asymmetry of the submarine canyon's banks in its middle reach is due to the combined action of recurrent slope instability and turbidity currents. In addition, two fields of sediment waves were identified in the study area. Field 1 is located on the south-west levée of the canyon and is fed by turbidity currents from one of its branches, being also associated with marked hydraulic jumps. Field 2 is observed in the southern bank of the lower canyon reach and was formed by the overspill of turbidity currents within the Taiwan Canyon due to the effect of inertial centrifugal forces. Turbidity currents sourced from Dongsha Channel also contributed to forming Field 2. Importantly, trains of plunge pools have been identified along the thalweg of the lower canyon reach, generated by turbidity currents deriving from the submarine canyons in the north of the Taiwan Canyon. These results not only provide a very detailed account of submarine bedforms within and around a large submarine canyon, but also contribute to a better understanding of their origin and development. The high-resolution bathymetric and seismic data in this work reveal how gravity flows can drive erosion and deposition in submarine canyons.

Keywords Plunge pools, sediment waves, slope failures, South China Sea, Taiwan Canyon, turbidity currents.

INTRODUCTION

Sediment gravity flows, usually occurring as submarine landslides and turbidity currents, are ubiquitous on both passive and active continental margins (Talling *et al.*, 2012). Submarine landslides can generate enormous turbidity currents and mass-transport deposits, or MTDs (Nisbet & Piper, 1998); they both play significant roles in eroding continental shelves and slopes, leading to the incision of submarine canyons while transporting large volumes of sediment into deep-sea environments (Canals *et al.*, 2006; Talling *et al.*, 2012). In addition, sediment gravity flows can generate widespread seafloor bedforms within and around submarine canyons, including vast fields of sediment waves (Kostic, 2014; Symons *et al.*, 2016; Normandeau *et al.*, 2018), seafloor scours (Lamb *et al.*, 2008; Covault *et al.*, 2014), troughs and plunge pools (Paull *et al.*, 2011; Schnyder *et al.*, 2018).

Large submarine canyons have been documented on the northern South China Sea margin, where sediment gravity flows play a vital role in their morphological development. Key examples are the Central Canyon in the Qiongdongnan Basin (Gong *et al.*, 2011; Li *et al.*, 2013), the Pearl River Canyon (Ding *et al.*, 2013; Wang *et al.*, 2017) and the multiple slope-confined canyons of the Pearl River Mouth Basin (Gong *et al.*, 2013) (Fig. 1). The Central Canyon was formed by the incision of large-scale gravity flows (slumps, debris flows and turbidity currents), which started in the Late Miocene (5.5 Ma) (Li *et al.*, 2013). Two main phases of Quaternary mass-wasting have been recognized in the middle segment of the Pearl River Canyon, indicating that MTDs played a significant role in its development (Wang *et al.*, 2017). There is also a clear asymmetry in the sub-linear, slope-confined canyons of the Pearl River Mouth Basin, as shown by their steep eastern walls and stepped, curved western walls sculpted by slumps and slides (Ding *et al.*, 2013; He *et al.*, 2014). Yin *et al.* (2019) link the asymmetry of these submarine canyons to contour currents, as well as to turbidity currents.

The Taiwan Canyon (also called South Taiwan Shoal Canyon or Taiwan Bank Canyon) is one of the largest submarine canyons on the north-eastern South China Sea margin, reaching a total length of *ca* 220 km (Ding *et al.*, 2010; Xu *et al.*, 2014; Zhong *et al.*, 2015) (Fig. 1). Using two-dimensional seismic and bathymetric data, Ding *et al.* (2010) revealed that the Taiwan Canyon was initiated in the Middle Miocene, and tectonic structures (i.e. a transform fault and seamount) have affected its orientation since then. The origin and development of Taiwan Canyon were also investigated, and high sediment supply, frequent gravity sliding (slumping) and faulting were considered as the main controlling factors (Xu *et al.*, 2014). Four fields of sediment waves are reported on the north-east South China Sea and three of them are located around the Taiwan Canyon (Gong *et al.*, 2012; Kuang *et al.*, 2014; Gong *et al.*, 2015; Yin *et al.*, 2015). Recent studies have documented the complex morphology of scours along its thalweg, interpreting them as cyclic steps resulting from the interaction of supercritical turbidity currents with the seafloor (Zhong *et al.*, 2015).

This paper focuses on the sediment gravity flows of the north-east South China Sea and their roles in the morphological development of the Taiwan Canyon. Sediment gravity flows occur frequently within and around the Taiwan Canyon due to the frequent earthquakes that affect the Manila Trench (Liu *et al.*, 2013). Seasonal typhoons are also capable of triggering turbidity currents in this region (Zhang *et al.*, 2018). This study investigates the morphological features within and around the Taiwan Canyon in greater detail than previous publications (Fig. 2A and B). Although sediment wave fields around the Taiwan Canyon have been recognized in previous work (Gong *et al.*, 2012; Kuang *et al.*, 2014), their origin and formation mechanisms are still poorly understood. This paper reveals for the first time that levées in the middle reach of Taiwan Canyon are asymmetrical and that a narrow (*ca* 1.6 km wide), elongated (*ca* 42 km long) trough with a west–east orientation occurs in the lower reach of Taiwan Canyon. This latter trough has not been identified in the published literature. Hence, a comprehensive analysis of submarine features and structures within and around the Taiwan Canyon is presented in this work with the ultimate aim of:

1 Investigating the factors controlling the asymmetry of the middle reach of the Taiwan Canyon.
2 Determining the processes responsible for the formation of sediment waves around the Taiwan Canyon.
3 Discussing how gravity flows can form erosional depressions in the lower reach of the Taiwan Canyon.

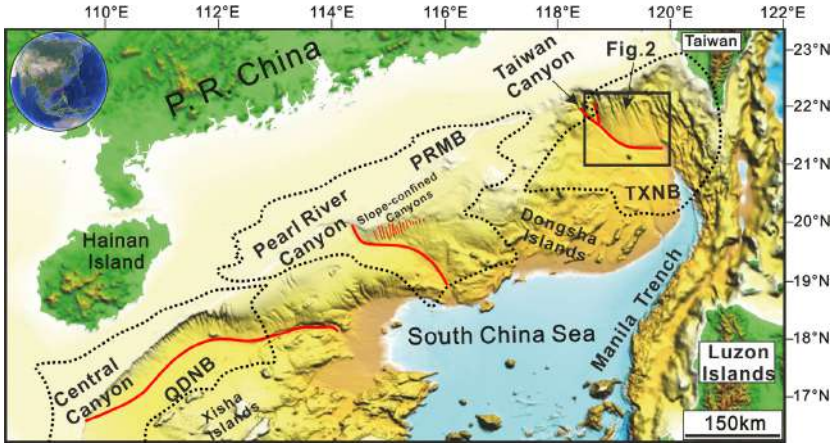

Fig 1. Detailed location of the study area in the South China Sea. The red lines represent the Central Canyon, Pearl River Canyon, slope-confined canyons and Taiwan Canyon from south-west to north-east. The black box indicates the location of Fig. 2. The dashed black lines represent the boundaries of the Qiongdongnan Basin (QDNB), Pearl River Mouth Basin (PRMB) and Taixinan Basin (TXNB). Major topographical features such as the Xisha Islands, Dongsha Islands and Manila Trench, are highlighted in the figure.

GEOLOGICAL SETTING

The South China Sea (SCS) is a wedge-shaped marginal sea whose oceanic crust is wider in its eastern part, narrowing down towards the south-west (Taylor & Hayes, 1983; Hsu *et al.*, 2004). Passive rifting in the SCS was initiated in the Late Cretaceous by north–south crustal extension (Wang *et al.*, 2006). A Late Oligocene to Middle Miocene phase of seafloor spreading followed the initial stages of continental rifting and was associated with progressive continental breakup along the SCS (Taylor & Hayes, 1983; Zhao *et al.*, 2016).

The study area is located to the north-west of the Taixinan Basin at a water depth of 200 to 3500 m, in the north-east SCS (Figs 1 and 2A). The Taiwan Canyon started to form in the Late Miocene (Ding *et al.*, 2010; Xu *et al.*, 2014; Liao *et al.*, 2016). During the Pliocene, the Taiwan Canyon served as the main sediment conduit transporting terrestrial coarse-grained sediment onto deep-water depocentres (Liao *et al.*, 2016), and was shifted eastward to converge with the Manila Trench during the late Pleistocene (Liao *et al.*, 2016). At this time, the ancient Hanjiang River flowed through the present-day continental shelf to transport fluvial sediments directly to the Taiwan Canyon (Xu *et al.*, 2014).

A left-lateral transform fault, called the Luzon–Ryukyu Transform Fault (LRTF), is located in the southern part of the Taiwan Canyon (Fig. 2B). The LRTF is revealed by changes in the trend of magnetic anomalies on the ocean floor, as well as changes in seafloor bathymetry and basement relief (Sibuet *et al.*, 2002; Hsu *et al.*, 2004). The fault connects the former south-east-dipping Manila Trench with the north-west-dipping Ryukyu Trench. In the Early Miocene, the LRTF became inactive due to the formation of the Luzon Arc and the onset of seafloor spreading in the eastern SCS between 20 Ma and 18 Ma (Hsu *et al.*, 2004). In addition to the LRTF, a seamount lies in the north-western region of the Taiwan Canyon (Fig. 2B). This seamount was formed during the Early Miocene (21 to 22 Ma) as revealed by the $^{40}Ar/^{39}Ar$ dating of its alkali basaltic rocks (Wang *et al.*, 2012).

DATA AND METHODS

Bathymetric and seismic data

Multibeam bathymetric and multichannel seismic data are used as the primary datasets in this work. These bathymetric data were acquired onboard the *R/V Sonne* during the joint Chinese–German Cruise 177, June 2004, using a SIMRAD EM120 multi-beam echo-sounder system (Kongsberg Maritime AS, Norway). The horizontal and vertical resolutions of the bathymetric data are *ca* 100 m and 3 to 6 m,

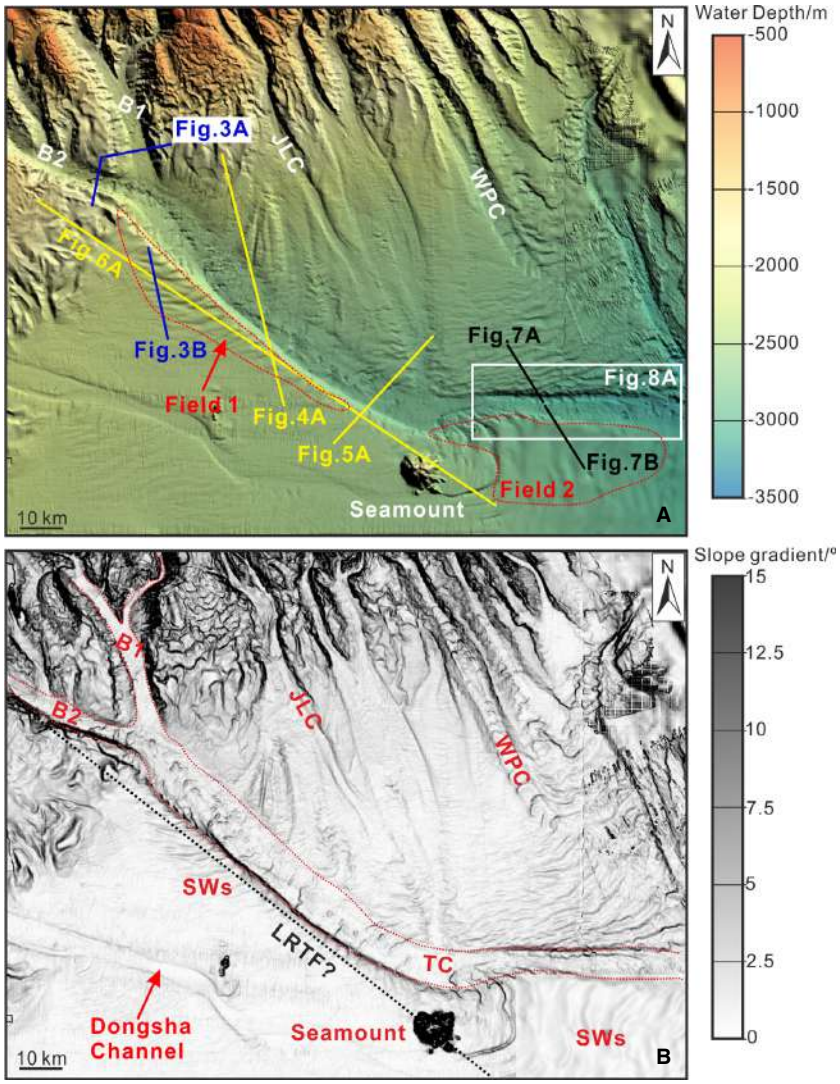

Fig 2. (A) High-resolution multibeam bathymetric map of the study area showing several submarine canyons with large gullies in their heads. Two blue solid lines in the upper and middle reach of Taiwan Canyon represent seismic profiles shown in Fig. 3A and B. Two shorter yellow solid lines highlight the levée asymmetry of the Taiwan Canyon shown in Figs 4A and 5A. The yellow solid line in the middle reach of Taiwan Canyon marks the location of the seismic profile in Fig. 6A. The white box represents the location of Fig. 8A. (B) Slope gradient map of the study area. The black dotted line represents the potential location of Luzon–Ryukyu Transform Fault (LRTF). The red dotted lines indicate the rims of Taiwan Canyon. B1: Branch 1; B2: Branch 2; SW: sediment waves; TC: Taiwan Canyon; JLC: Jiulong Canyon; WPC: West Penghu Canyon.

respectively. The multibeam bathymetric data were imported and analyzed in Global Mapper®.

Multichannel seismic data are used to characterize near-seafloor bedforms around the Taiwan Canyon. Two long seismic-reflection profiles [MGL0905-05 (*ca* 70 km) and MGL0905-10 (*ca* 41 km)], acquired as part of the Taiwan Integrated Geodynamic Research (TAIGER) project, are also used in this work, together with an additional two-dimensional (2D) multichannel seismic profile acquired by the South China Sea Institute of Oceanology, Chinese Academy of Sciences, in May 2019 (Fig. 2A). The frequency bandwidth of this latter seismic profile is 30 to 45 Hz, providing an average vertical resolution of 11 to 17 m for shallow strata. The seismic profile was acquired by an 1800 m long streamer with 144 channels and spaced 12.5 m. The seismic profile was processed using RadExpro® and interpreted on Geoframe®.

Calculations of turbidity current properties

The flow properties of turbidity currents flowing through the sediment wave fields were calculated based on the morphological parameters of the sediment waves identified in seismic and bathymetric data. These morphological parameters include the wavelength and the slope gradient of the lee and stoss sides of sediment waves, which are used in several equations to calculate:

1 the internal Froude number (F_i) of turbidity currents using the slope gradient (α), drag

coefficient at the bed (C_f) and entrainment coefficient at the upper interface (e), as represented by Eq. 1;

2 the flow thickness (h) using the relationship between wavelength (L) and the internal Froude number (F_i) in Eq. 2;

3 the velocity of sediment waves in the stoss and lee sides using $\Delta\rho$ (grain density – density of turbidity currents/seawater density), C (the volume concentration), g (gravitational acceleration), internal Froude number (F_i) and flow thickness (h):

$$F_i^2 = \frac{\sin(\alpha)}{C_f + e} \tag{1}$$

$$h = \frac{L}{2\pi F_i^2} \tag{2}$$

$$u^2 = \Delta\rho C g h F_i^2 \tag{3}$$

where F_i is the internal Froude number of turbidity currents and α is slope gradient of sediment waves. Suggested values for the drag coefficient C_f of turbidity currents range from 3.5×10^{-3} to 4×10^{-3} (Bowen *et al.*, 1984). The lowest value of 3.5×10^{-3} is more applicable to unconfined flows (Wynn *et al.*, 2000). The entrainment coefficient e for most turbidity currents varies between 5×10^{-4} and 6×10^{-3}, while sediment concentration (C) is a dimensionless number ranging from 5×10^{-5} to 5×10^{-4} (Piper & Savoye, 1993). The parameter g represents the gravitational acceleration, considered to be 9.81 m s^{-2}.

This work calculated the Froude numbers of circular depressions within the Taiwan Canyon, before and after hydraulic jumps, using Eqs 4 and 5:

$$\mathrm{Fr}_1 = \frac{u}{\sqrt{\Delta\rho C g h}} \tag{4}$$

$$\mathrm{Fr}_2 = \frac{2^{1.5}\mathrm{Fr}_1}{\left(\sqrt{1 + 8\mathrm{Fr}_1^2} - 1\right)^{1.5}} \tag{5}$$

where the sediment concentration (C) is the volume sediment concentration and g is the gravitational acceleration (9.81 m s^{-2}). The parameter h is the flow depth of turbidity currents and u represents the velocity of turbidity currents; $\Delta\rho$ represents the difference sediment density – density of turbidity currents/seawater density.

RESULTS

Morphological evolution of the Taiwan Canyon

The Taiwan Canyon is observed at a water depth ranging from 500 to 3500 m (Fig. 2A). It is approximately 220 km long and 6 to 12 km wide (Fig. 2A and B). In bathymetric data, Branch 1 is located in the northern part of the Taiwan Canyon at a water depth between 2000 to 2500 m, while Branch 2 is oriented north-west/south-east and occurs at a water depth of 2100 to 2500 m (Figs 2A and 3A). Branch 1 is 7 km wide and *ca* 42 km long, while Branch 2 is 6 km wide and 40 km long (Fig. 2A).

The middle reach of the Taiwan Canyon is *ca* 80 km long and is observed at a water depth of 2500 to 3125 m. Here, its banks are asymmetrical in both their height and slope gradient (Figs 4A, 4B, 5A and 5B). The south-west bank of the Taiwan Canyon is steeper than its north-east counterpart; the slope gradient of the south-west bank ranges from 6.5 to 13°, but it ranges from 1 to 2° on the north-east bank (Figs 4B and 5B). Moreover, the south-west bank of the Taiwan Canyon is higher than its north-east counterpart (*ca* 300 m and 230 m high, respectively) (Figs 4B and 5B). Along the middle reach of the Taiwan Canyon, MTDs are identified on the seismic profiles, appearing as discontinuous, transparent reflections (Figs 4C and 5C). These MTDs occur along the base of the continental slope in Pliocene and Pleistocene strata (Liao *et al.*, 2016), indicating complex 'cut and fill' processes during the development of Taiwan Canyon.

The lower reach of the Taiwan Canyon is *ca* 60 km long and occurs at a water depth of 3125 to 3500 m (Fig. 2A). The Taiwan Canyon changes its orientation from north-west/south-east to nearly east–west at a water depth of 3070 m (Fig. 2A and B). A seamount is located to the south-west part of the canyon at a water depth of 2750 m. The seamount is 1200 m high and 6 to 8 km wide, spanning *ca* 70 km^2 of the continental slope (Fig. 2A and B).

Sediment wave fields around the Taiwan Canyon

Two fields of sediment waves are observed around the Taiwan Canyon (Figs 2A and 6A). Field 1 spans the south-west levée in the middle reach of Taiwan Canyon at a water depth of

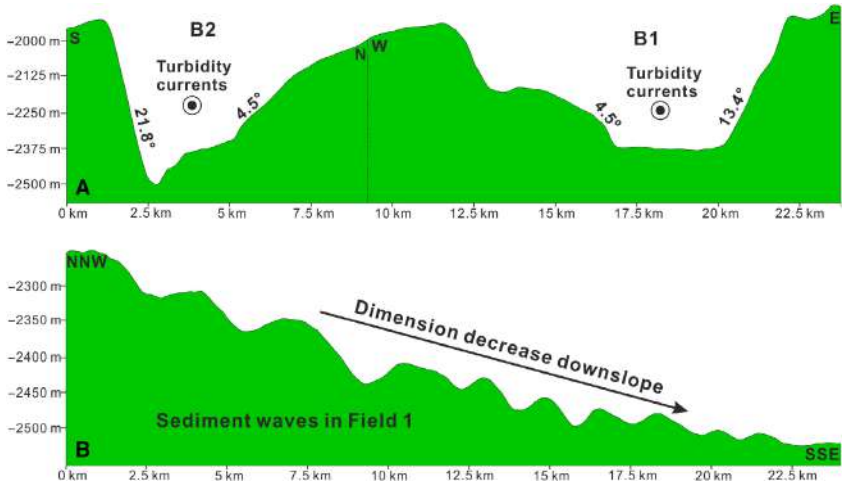

Fig 3. (A) Bathymetric profile illustrating two branches (B1 and B2) in the upper reach of Taiwan Canyon. (B) Bathymetric profile showing the sediment waves in Field 1 and their dimensions (wavelengths and wave heights) decrease downslope.

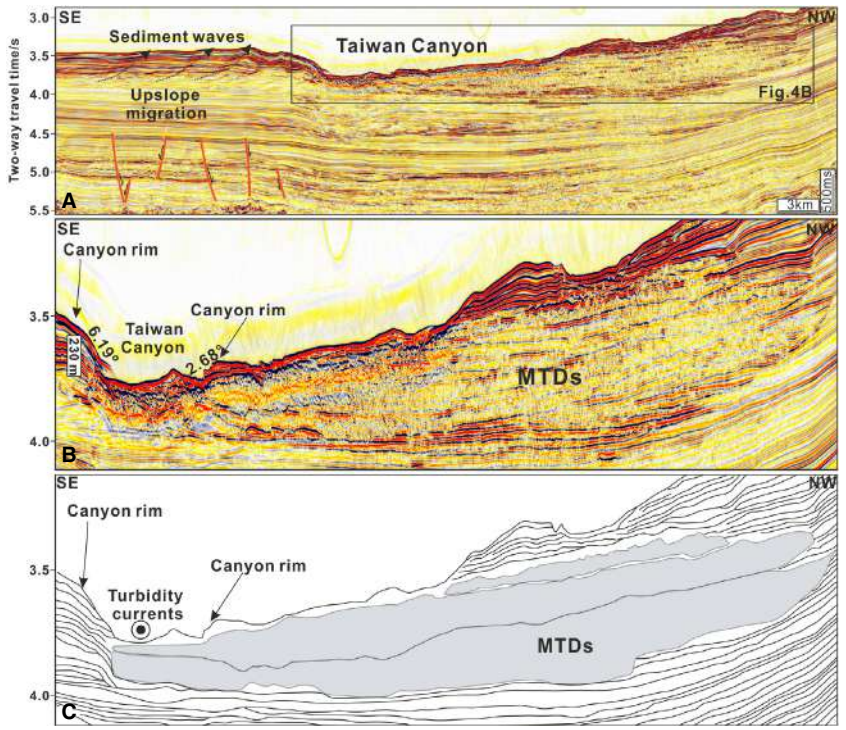

Fig 4. (A) Two-dimensional (2D) seismic profile of the Taiwan Canyon highlighting the morphological differences in canyon banks shown in Fig. 2. The black box indicates the location of the MTDs shown in (B). Note that the slope gradient and height of the south-west levée are larger than to the north-east. (B) The mass-transport deposits (MTDs) are characterized by chaotic amplitude reflections. The black arrows represent canyon rims. (C) Line-drawn interpretation of (B) illustrating the presence of widespread MTDs in the north-east of Taiwan Canyon. Note that the north-eastern flank of Taiwan Canyon was eroded by these MTDs.

2250 to 2840 m, with a slope gradient of 0.5° on average (Figs 2A, 2B and 6C). These sediment waves cover *ca* 510 km^2 of the levée and their dimensions (wavelengths and wave heights) become smaller with increasing water depth (Figs 2A, 3B and 5C). The wavelengths of sediment waves in Field 1 range from 1.2 km to 3.7 km and show wave heights of 30 to 47 m. The slope gradient ranges from 0.43 to 1.78° on the stoss sides of waves in Field 1, and 1.09 to 2.49° on their lee sides (Table 1). The crests of sediment waves are bifurcated and their orientation approaches west–east (Fig. 2B). The seismic reflections within the sediment waves are continuous and can be traced from one wave to another (Fig. 6C). Discrete sediment waves show asymmetrical geometries with a long and thicker upslope flank but a short and thinner downslope flank, and their crests display a trend of upslope migration (Fig. 6C). This work estimates the velocities of turbidity currents flowing through Field 1 as comprising V_{stoss} from 2.16 m s^{-1} to

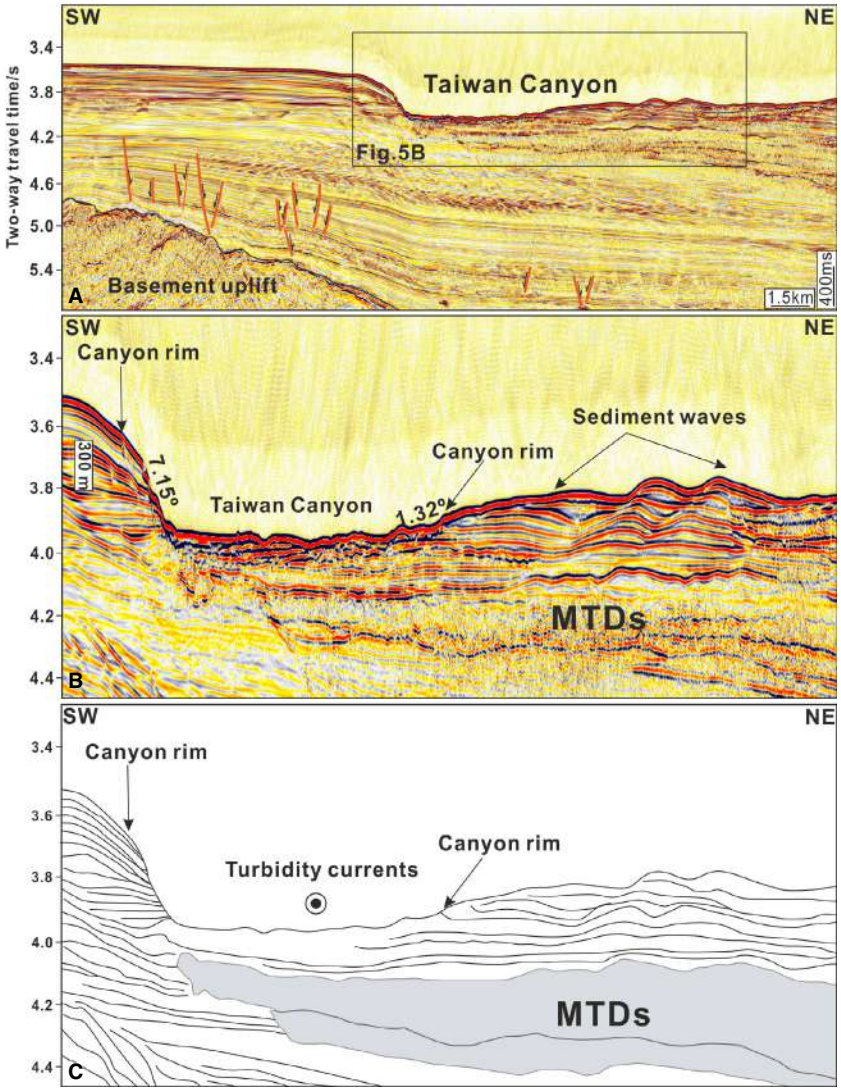

Fig 5. (A) Two-dimensional (2D) seismic profile of the Taiwan Canyon showing the morphological differences in canyon banks imaged in Fig. 2. The black box indicates the position of the mass-transport deposits (MTDs) shown in (B). (B) The MTDs are characterized by chaotic amplitude reflections. Note that the slope gradient and height of the south-west levée are larger than to the north-east. The black arrows point at canyon rims and sediment waves. (C) Line-drawn interpretation of (B) shows the internal architecture of the middle reach of Taiwan Canyon and numerous MTDs can be observed.

3.31 m s^{-1} and V_{lee} between 2.17 m s^{-1} and 3.4 m s^{-1}, based on Eqs 1 to 3 (Table 1).

Field 2 is located in the southern side of the Taiwan Canyon at a water depth between 3150 m and 3500 m (Fig. 2A). Here, slope gradient reaches 0.57° on average, but only the northern part of the Field 2 is fully imaged by this data set, covering a total area of 870 km^2. These sediment waves are almost perpendicular to the orientation of the Taiwan Canyon and reveal a north–south orientation (Figs 2B, 6B and 7B). Sediment waves show asymmetrical profiles in cross-section and marked upslope-migrating, sinuous, bifurcate crests (Fig. 7B). These waves' crests develop parallel in two trains. Waves in Field 2 have relatively large dimensions, with wavelengths ranging from 1.5 to 5.4 km and have wave heights ranging from 50 to 110 m.

Trough along the Taiwan canyon thalweg

Troughs are narrow, elongated depressions on the seafloor with flat bottoms and steep flanks (Heap & Harris, 2008). In the present study area, a new trough is identified in the lower reach of the Taiwan Canyon at a water depth from 3300 to 3500 m, where the slope gradient is 0.3° on average (Figs 2A, 8A and 8B). It extends for *ca* 44 km with a west–east orientation and has a width of *ca* 1.6 km, covering about 72 km^2 of the continental slope (Fig. 8A). This trough is close to the north bank of the lower reach of the Taiwan Canyon, and sediment waves are located further to the north (Figs 8A, 8B, 9A and 9C). It has an incision depth of *ca* 100 m on average, and shows several undulations in cross-section and closed circular-shaped depressions in plan

view (Fig. 8A and C). These depressions are 1.38 to 3.86 km in diameter and 62.0 to 119.1 m in height (Fig. 8C; Table 2). Moreover, marked differences in slope gradient can be observed on the walls of the lower reach of the Taiwan Canyon (Fig. 9B and D). The slope gradient of the northern canyon wall of these depressions ranges from 6.3 to 12.4°, while it varies from 3.2 to 14.3° on the southern canyon wall (Table 2).

Table 1. Sediment waves (SWs) in Field 1.

SWs	Stoss side (km)	Lee side (km)	Stoss side (°)	Lee side (°)	u_{stoss} (m s^{-1})	u_{lee} (m s^{-1})
1	1170	1234	0.43	2.32	3.311	3.400
2	805	2416	0.66	2.19	2.746	4.757
3	905	1661	1.29	1.09	2.912	3.945
4	729	968	1.23	2.49	2.613	3.011
5	692	951	1.19	2.35	2.546	2.985
6	665	943	1.78	1.15	2.496	2.972
7	641	981	1.13	1.41	2.450	3.031
8	478	503	0.76	1.30	2.160	2.171

DISCUSSION

Controls on the asymmetry of the middle reach of Taiwan canyon

Asymmetrical submarine canyons have been widely observed when analyzing slope gradient and the height of canyon banks on cross-sectional bathymetric profiles (Mountjoy *et al.*, 2009; Micallef *et al.*, 2014). These asymmetrical canyons have been suggested to result from regional tectonics (Dantec *et al.*, 2010; Micallef *et al.*, 2012), the effect of the Coriolis force (Cossu *et al.*, 2010; Cossu *et al.*, 2015), gravity flows (Keevil *et al.*, 2007; Arzola *et al.*, 2008) and contour currents acting on the continental slope (Fonnesu *et al.*, 2020; Miramontes *et al.*, 2020). In the study area, a prominent asymmetry in the Taiwan Canyon is documented not only by the recorded difference in its bank height, but also by analyzing slope gradients in its middle reach (Figs 4B and 5B). Several potential controls on the asymmetry of the middle reach of Taiwan Canyon are discussed below.

Local tectonic structures such as folds and faults directly affect the location, alignment and geometry of many submarine canyons (Dantec *et al.*, 2010; Micallef *et al.*, 2014). Several researchers have proposed the south-west levée of the middle reach of Taiwan Canyon to be part of a major transform plate boundary, the Luzon–Ryukyu Transform Fault (Sibuet *et al.*, 2002; Hsu *et al.*, 2004; Yeh *et al.*, 2010). It appears that the orientation of the Taiwan Canyon is parallel to the Luzon–Ryukyu Transform Fault (LRTF). However, the Luzon–Ryukyu Transform Fault cannot be clearly identified on the seismic profiles across the Taiwan Canyon,

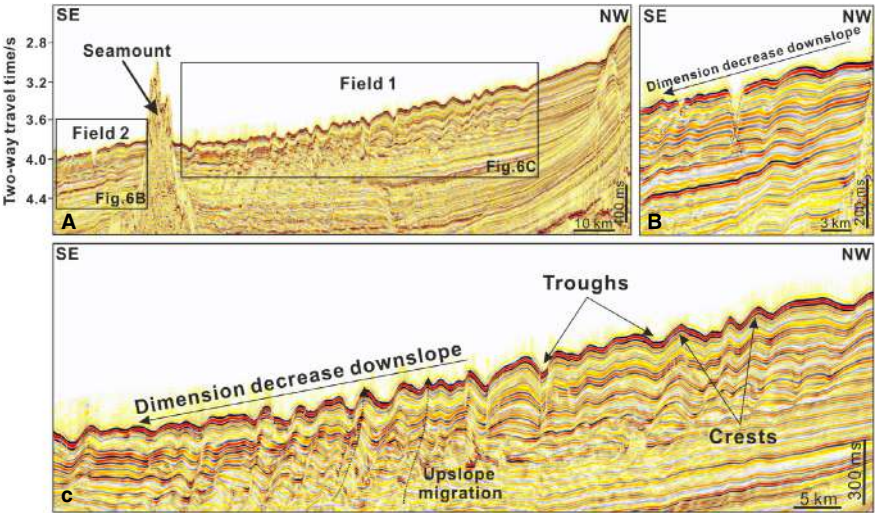

Fig 6. (A) Two-dimensional (2D) multichannel seismic profile across an area with sediment waves in Fields 1 and 2 (see Fig. 2 for location). The black box indicates the location of Fields 1 and 2 as shown in (C) and (B), respectively. (B) Upslope migration in sediment waves comprising Field 2. Downslope decrease is shown in the dimension of sediment waves in Field 2. (C) Upslope migration and downslope decrease of dimension in sediment waves comprising Field 1.

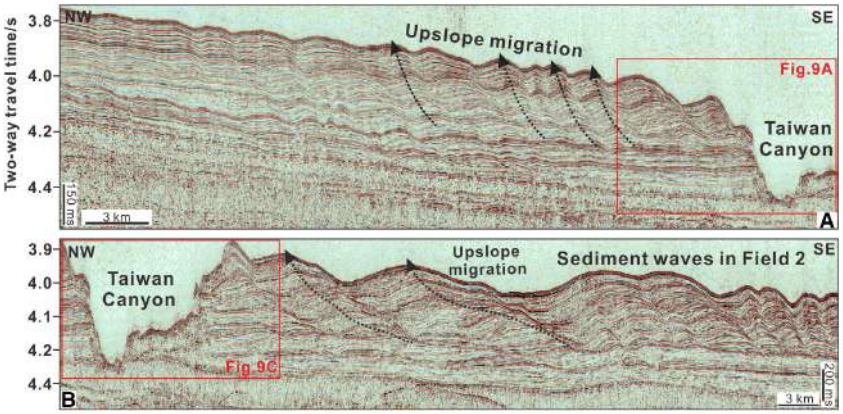

Fig 7. (A) Two-dimensional (2D) multi-channel seismic profile of the seismic line modified from Gong *et al.* (2012). See Fig. 2 for location. The red box indicates the trough (elongated depression) shown in Fig. 9A. (B) 2D multi-channel seismic profile of the seismic line modified from Gong *et al.* (2012) in Fig. 2. The red box indicates the trough shown in Fig. 9C.

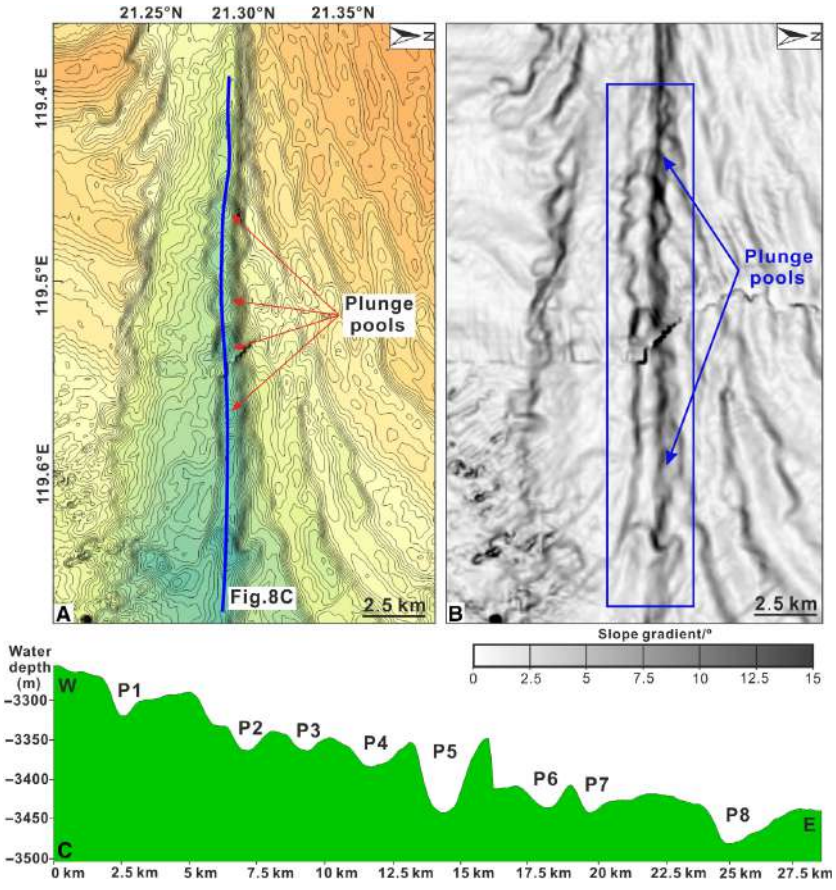

Fig 8. (A) Contour map in the lower reach of Taiwan Canyon showing trains of plunge pools. The blue line indicates the cross-section profile of plunge pools shown in (C). (B) Slope gradient map illustrates the presence of numerous plunge pools within the trough. The blue box shows the distribution of plunge pools. (C) Cross-sectional bathymetric profile of the plunge pools shown in (A). Eight plunge pools are observed from east to west at a water depth from 3300 to 3500 m.

and there is also no obvious fault close to the south-west bank of this canyon (Figs 4A and 5A). A series of normal faults occur only in much deeper strata (4.5 s to 5.8 s TWTT – two-way travel time), not influencing the asymmetry of the middle reach of Taiwan canyon (Figs 4A and 5A). Therefore, this study proposes that regional tectonics affected the orientation of Taiwan Canyon but did not control the asymmetry observed in its middle reach.

In the Northern Hemisphere, the Coriolis force laterally deflects turbidity currents so that both their density interface and downstream velocity maxima are deflected to the right-hand side of submarine canyons in a downstream direction (Cossu *et al.*, 2010). This shift in flow

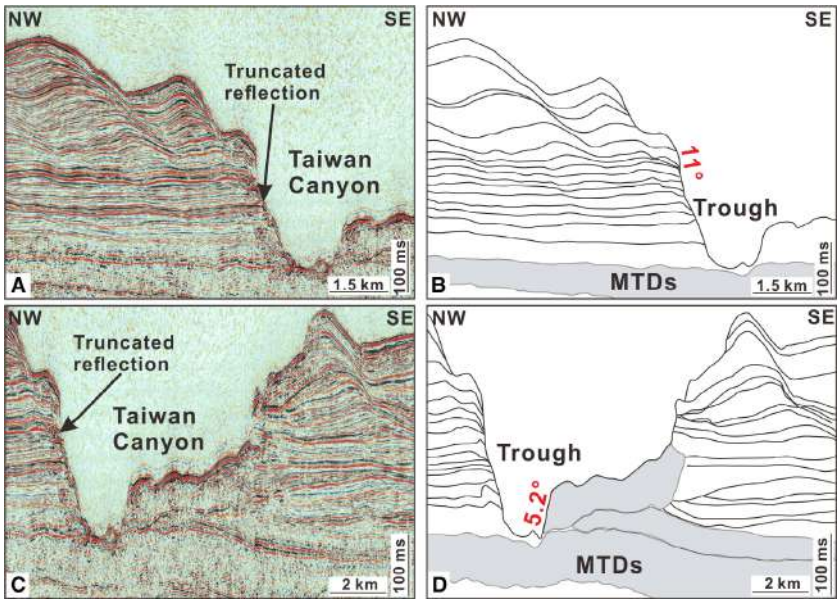

Fig 9. (A) Two-dimensional (2D) multi-channel seismic profile of the trough in Fig. 7A. Truncation reflections are observed on the seismic profile. Truncations can be observed on both sides of the trough. (B) Line-drawn interpretation of (A) outlining the internal architecture of trough and mass-transport deposits (MTDs). (C) Two-dimensional (2D) multi-channel seismic profile of the trough shown in Fig. 7B. Erosional truncation (truncated reflections) is observed on the seismic profile. (D) Line-drawn interpretation of (C) showing the internal character of trough at the bottom of Taiwan Canyon. The grey blocks indicate the recurrent MTDs.

Table 2. Morphological characteristics of plunge pools.

Plunge pools	Width (longitudinal section) (km)	Width (cross-section) (km)	Height (m)	Slope gradient (N) (°)	Slope gradient (S) (°)
1	1.38	1.68	75.40	9.36	4.39
2	1.92	1.61	61.90	10.98	8.69
3	1.77	2.00	80.10	10.23	5.69
4	2.79	1.68	68.76	9.20	6.31
5	2.88	1.64	119.18	12.04	14.26
6	1.97	2.01	95.40	10.99	8.08
7	1.41	1.71	67.44	6.33	7.88
8	3.86	2.16	86.08	12.42	3.21

orientation can change the loci of erosion and deposition on continental slopes, and consequently impose differences in canyon bank height and slope gradient (Cossu & Wells, 2013; Cossu *et al.*, 2015). The ratio between the Coriolis force and the inertial force of gravity flows in submarine canyons is represented by the Rossby number (Cossu *et al.*, 2015).

Turbidity currents flowing south-east along the Taiwan Canyon are affected by the Coriolis force, resulting in enhanced erosion and therefore larger slope gradients in the south-west side of its middle reach. However, the Coriolis force may not impose great differences in canyon bank height due to the large Rossby number ($|Ro|>10$) recorded in low latitude areas (Cossu *et al*, 2010). In the study area herein, at a latitude of 21°N, the Rossby number ranges from 10 to 20, suggesting that the Coriolis force is not the main reason for the difference in canyon bank height recorded in the middle reach of the Taiwan Canyon.

Gravity flows such as submarine landslides are ubiquitous in deep-sea environments, and are the dominant processes eroding the continental slope and enlarging submarine canyons (Pratson & Coakley, 1996). Recurrent MTDs are identified in the north-east overbank of the middle reach of Taiwan Canyon (Figs 4B and 5B); they are relatively younger than the Taiwan Canyon (Liao *et al.*, 2016). The presence of stacked MTDs indicates that the north-east bank of Taiwan Canyon was eroded by slope failures originating from the area to the north-east (Figs 4B and 5B). This leads to the differences in canyon bank height in the middle reach of the Taiwan Canyon.

The simultaneous interaction of contour and turbidity currents on continental slopes can result in asymmetrical canyon–levée systems (Gong *et al.*, 2018; Fonnesu *et al.*, 2020; Miramontes *et al.*, 2020), especially in the zones where the downslope turbidity currents have velocities of 2 m s^{-1} or less, and where submarine channels are not deeply incised (Miramontes *et al.*, 2020). The velocity of turbidity currents in the middle reach of Taiwan Canyon ranges from 4 to 10 m s^{-1} (Zhong *et al.*, 2015), values that are 40 to 100 times larger than that of contour currents (*ca* 15 cm s^{-1} on average), as documented by Zhao *et al.* (2016) in the same area. First, contour currents may not have a marked effect on the deflection of turbidity currents that flow along the Taiwan Canyon towards the south-east. In addition, the differences in water depth between the thalweg and south-west levée in the middle reach of Taiwan Canyon are *ca* 300 to 400 m (Fig. 10),

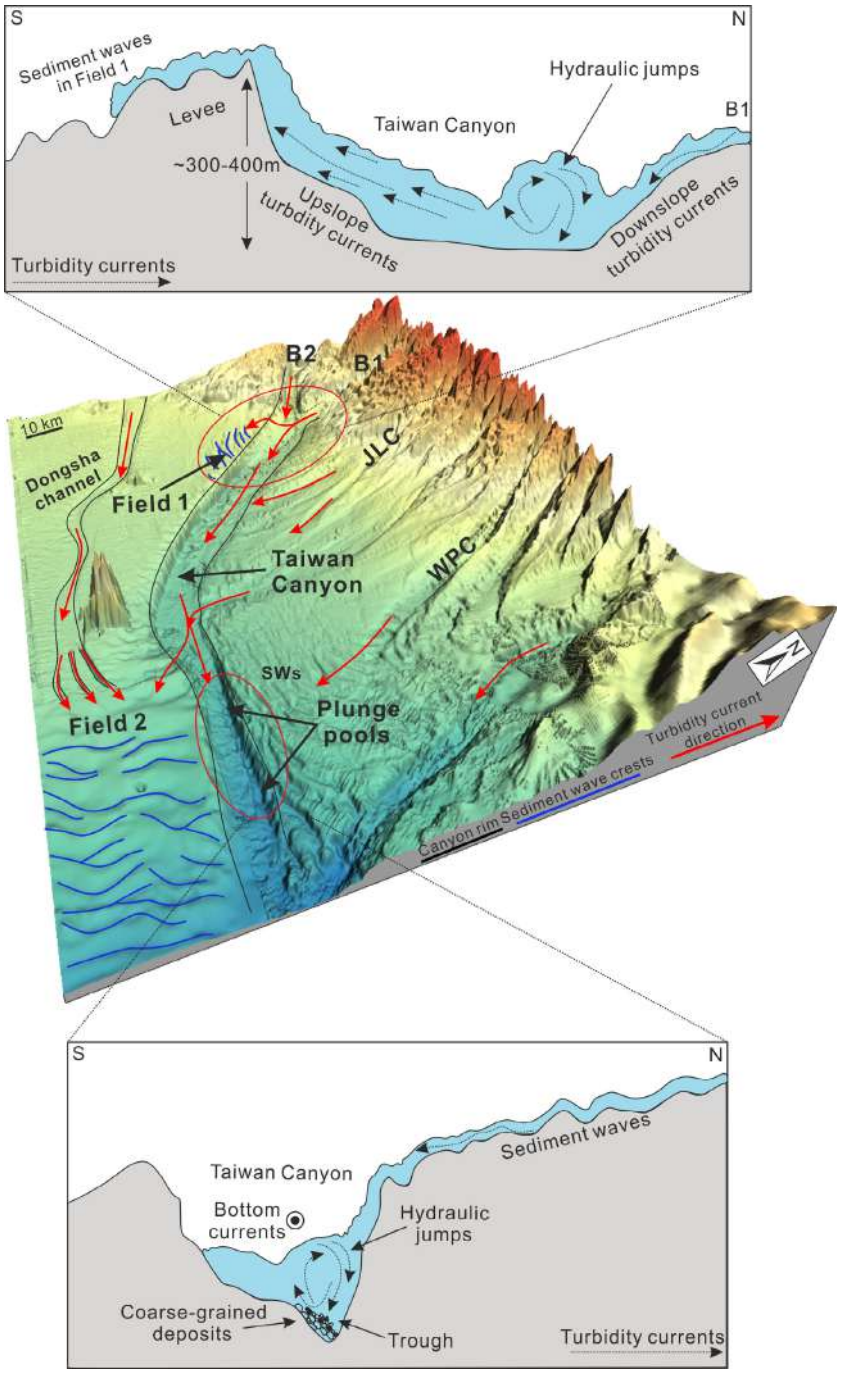

Fig 10. Three-dimensional view of the morphological features within and around the Taiwan Canyon, including the sediment waves in Fields 1 and 2, and plunge pools in the lower reach of Taiwan Canyon. Schematic diagrams summarize the formation mechanisms of sediment waves in Field 1 and plunge pools in the lower reach of Taiwan Canyon. The dark grey lines indicate the position of the canyon rim, while the blue lines indicate the crests of sediment waves. The red arrows illustrate the direction of turbidity currents. B1: Branch 1; B2: Branch 2; SWs: sediment waves; JLC: Jiulong Canyon; WPC: West Penghu Canyon.

and such a difference in levée height can prevent the overspill of turbidity currents from Taiwan Canyon.

In summary, this study suggests that erosion by recurrent slope failures to the north-east of the Taiwan Canyon is the main reason for the contrast in canyon bank heights (about 300 m on average). However, it also suggests that the observed differences in slope gradient on both banks of the Taiwan Canyon result mainly from the erosion of turbidity currents along the canyon which are heavily influenced by inertial centrifugal forces.

Mechanisms forming sediment waves around the Taiwan Canyon

Based on the interpretation of the multibeam bathymetric map and two-dimensional seismic profiles used in this study, two fields of sediment waves can be identified around the Taiwan Canyon (Fig. 2A and B). The sediment waves in the lower reach of Taiwan Canyon are not the focus in this work because they have been proposed to be generated by unconfined turbidity currents flowing out of the West Penghu Canyon (Gong *et al.*, 2012; Kuang *et al.*, 2014). The formation of deep-water sediment waves has been attributed to multiple causes, including downslope turbidity currents (Wynn & Stow, 2002; Covault *et al.*, 2014), along-slope contour (bottom) currents (Masson *et al.*, 2002; Betzler *et al.*, 2014), interactions between turbidity and contour currents (Normandeau *et al.*, 2018) and submarine landslides (Hampton *et al.*, 1996; Pope *et al.*, 2018; Casalbore *et al.*, 2020). In the following sections, the formation mechanisms of sediment waves in Fields 1 and 2 are analyzed in detail.

Four key observations comprise key evidence to determine the formation mechanism of sediment waves in Fields 1 and 2.

1 The crests of sediment waves in Fields 1 and 2 are parallel to the bathymetric contours (Fig. 2A). Wynn & Stow (2002) have proposed that crests of sediment waves formed by bottom currents are usually aligned at a low angle (typically 10 to 50°) to the regional contours, while the crests of sediment waves generated by turbidity currents on submarine slopes are normally parallel to these latter. This indicates that the sediment waves in Fields 1 and 2 cannot solely be produced by bottom currents.

2 The wave crests are sinuous and bifurcate in plan view and they are oblique to the orientation of Taiwan Canyon in its middle reach (Fig. 2A and B). In areas with good planform coverage most turbidity current sediment waves appear as linear features with varying degrees of sinuosity and/or bifurcation (Wynn & Stow, 2002; Symons *et al.*, 2016), suggesting a turbidity current of origin for the sediment waves of Fields 1 and 2.

3 The dimensions (wavelengths and wave heights) of sediment waves in Fields 1 and 2 decrease downslope in a gradual way (Figs 3B, 6B and 6C). This is an important observation because sediment waves formed by turbidity currents are usually smaller in a downslope direction due to decreasing sediment supply and flow velocity downslope (Normark *et al.*, 2002). In contrast, bottom current sediment waves are irregular with no consistent change in wave dimensions (Wynn & Stow, 2002).

4 Discrete seismic reflections within the sediment waves are continuous and can be traced across the troughs from one wave to the next (Fig. 6B and C). Although seismic reflection patterns in the wave troughs can mimic fault planes in some cases, sediment waves formed by turbidity currents or bottom currents consist of continuous, parallel or sub-parallel reflections on both sides (Lee *et al.*, 2002). In comparison, submarine landslides or creep folds show clear displacement along fault planes, especially in their troughs (Hill *et al.*, 1982; Lee & Chough, 2001). Such a character suggests that submarine landslides may not result in the formation of sediment waves in Fields 1 and 2. As discussed above, the sediment waves in Fields 1 and 2 are most likely generated by turbidity currents.

The crests of sediment waves are considered to align perpendicular to the flow direction of turbidity currents (Wynn & Stow, 2002). The wave crests in Field 1 are west–east oriented and this reveals that turbidity currents were sourced from Branch 1 of the Taiwan Canyon. Thus, turbidity current stripping is considered to have occurred from the main flow in the Taiwan Canyon. The stripped turbidity current flowed over the southern levée in a series of hydraulic jumps, leading to the generation of sediment waves in Field 1 (Fig. 10). Overspilling turbidity currents have been documented in the Monterey East Channel (Fildani *et al.*, 2006) and the Eel Canyon offshore California, USA (Lamb *et al.*, 2008), where sediment waves are widely distributed. Additionally, the observed overspilling turbidity currents in Eel Canyon and Monterey East Channel show a gradual decrease

in their velocities, and consequently result in the reduction in sediment waves' dimensions.

The wave crests in Field 2 are observed to be sinuous and bifurcate on the bathymetric map, and are more complex when compared with wave crests in Field 1 (Figs 2A and 10). The bifurcation and sinuosity of wave crests suggest an interaction of turbidity currents from different areas (e.g. Wynn *et al.*, 2000). Moreover, these wave crests extend in a north–south or north-east/south-west direction and they develop as two trains (Figs 2B and 10). This phenomenon indicates that turbidity currents may be derived from the north or north-west of Field 2. Hence, two possible sources of turbidity currents that may overspill into this field of sediment waves are proposed here. The most likely source is the overspill of turbidity currents from the Taiwan Canyon due to inertial centrifugal forces. In addition, the Dongsha Channel is located to the west of sediment waves in Field 2, and there might be turbidity currents flowing through this channel. These flows are initially constrained within a confined environment, but rapidly become unconfined downslope and spread out over an extensive area.

Origin and development of plunge pools within the lower reach of Taiwan Canyon

Plunge pools are defined as a series of discrete depressions and occur at sharp changes in slope gradient exceeding 4° (Lee *et al.*, 2002). They are widely distributed within submarine canyons on both active and passive continental margins (e.g. Betzler *et al.*, 2014; Schnyder *et al.*, 2018). In this study, several discontinuous depressions are located close to the north flank of the Taiwan Canyon in its lower reach (Fig. 8B). The depth of these depressions is much larger than documented in other areas (Table 3). They are shown as circular-shaped closed depressions on the contour map and are concave-shape in cross-section (Fig. 8A and C). Therefore, this study proposes that these depressions, observed in the lower reach of Taiwan Canyon, comprise plunge pools.

The formation of plunge pools in deep-sea environments is chiefly caused by: (i) sediment-laden density flows ('impact pools'); (ii) erosion by contour currents; or (iii) hydraulic jumps in turbidity currents ('hydraulic jump pools') (Lee *et al.*, 2002). Plunge pools generated by sediment-laden density flows often have larger slope gradients in their upslope bank (>20°) (Pratson & Coakley, 1996; Lee *et al.*, 2002). However, the plunge pools in the present study are characterized by slope gradients from 6.3 to 12.4° on their northern flank, values that are much smaller than the typical gradients of impact pools (Tables 2 and 3). Sediment-laden density flows should not be responsible for the generation of plunge pools in the study area. Because depressions created by contour currents are generally wider than plunge pools, they form elongated troughs instead of a series of discrete depressions (Stow *et al.*, 1998; Lee *et al.*, 2002). In this study, the plunge pools are north–south orientated (Figs 8B and 10), a direction perpendicular to the bottom currents flowing along the lower reach of Taiwan Canyon (Gong *et al.*, 2012; Liu *et al.*, 2016). This indicates that these plunge pools are unlikely to be formed by along-slope bottom currents.

The sharp change of calculated Froude numbers suggests that turbidity currents change their flow regime from supercritical to subcritical

Table 3. Comparison with plunge pools described in previous studies.

Location	Water depth (m)	Plunge pool depth (m)	Gradient break (°)	Scarp height (m)	Reference
Western Norwegian Sognefjord	800	25	12–18	800	Aarseth *et al.* (1989)
Submarine Bank Molokai, Hawaii	1650	90	–	35	Clague & Moore (2002)
Haida Gwaii Canyon, British Columbia	1000	4	12	–	Harris *et al.* (2014)
North-eastern Sicily Canyon	400	10–15	–	–	Gamberi *et al.* (2017)
Western Great Bahama Bank	177	22	16	120	Schnyder *et al.* (2018)
This study	3300	62–119	6–12	158–269	–

when passing over the bottom of plunge pools. Moreover, a sediment core collected on the southern edge of a Quaternary plunge pool indicates fine to medium-grained sands and silts ranging in grain size from 4Φ to 8Φ in the Krumbein phi scale (Gong *et al.*, 2012; Gong *et al.*, 2015). These two lines of evidence suggest that plunge pools are most likely formed by hydraulic jumps of turbidity currents. There are two sources of turbidity currents that may flow through plunge pools, including the turbidity currents (towards the east) within the Taiwan Canyon, and turbidity currents (towards the south) from the northern bank of Taiwan Canyon. If the plunge pools were generated by turbidity currents within the Taiwan Canyon, they would overspill to the south-east due to the occurrence of the seamount (Fig. 2A). They would be affected by the Coriolis force, resulting in enhanced erosion close to the south side of the lower reach of the Taiwan Canyon. These phenomena are inconsistent with the presence of a series of plunge pools adjacent to the northern bank of Taiwan Canyon's lower reach. Thus, turbidity currents might be sourced from the northern bank (for example, West Penghu Canyon) of the Taiwan Canyon (Fig. 7A and 10).

IMPLICATIONS

These results provide three main contributions towards a better understanding of sediment gravity flows (turbidity currents and submarine landslides) and their role on the morphological development of submarine canyons.

Turbidity currents are one of the most important, but also one of the least documented, sediment transport processes on Earth (Talling *et al.*, 2007; Paull *et al.*, 2018). They can strongly modify the seafloor morphology and generate various submarine bedforms (Talling *et al.*, 2007; Meiburg & Kneller, 2010). Frequent turbidity currents with high velocity (5 to 8 m s^{-1}) have been documented on the north-eastern South China Sea margin by *in situ* measurements (Zhang *et al.*, 2018). In this study, the velocity of turbidity currents is still 3 to 4 m s^{-1} after overspilling the south-west levée in the middle reach of Taiwan Canyon (*ca* 300 to 400 m), leading to the formation of sediment waves in Field 1 (Fig. 10). Several plunge pools are found in the lower reach of Taiwan Canyon. The origin and development of these plunge pools strongly suggests the powerful erosional ability of turbidity currents when entering the Taiwan Canyon. In contrast to the previous literature (Xu *et al.*, 2014; Kuang *et al.*, 2014; Yin *et al.*, 2015), this study succeeds in reporting numerous morphological features (sediment waves and plunge pools) within and around the Taiwan Canyon to reveal the role of turbidity currents on their development.

The dimensions (wavelengths and wave heights) of sediment waves are mainly controlled by the hydraulic characteristics of turbidity currents (for example, velocity, discharge and energy loss) (Wynn & Stow, 2002; Symons *et al.*, 2016). Although sediment waves have been reported on the south-west levée of middle reach of Taiwan Canyon in the published literature (e.g. Kuang *et al.*, 2014; Zhong *et al.*, 2015; Yin *et al.*, 2015), this study develops a quantitative analysis of their formation mechanism and proposes a schematic model for their development. This work contributes to a more complete understanding of flow dynamics in turbidity currents occurring around submarine canyons.

Submarine landslides can transport large volumes of sediment from the continental slope to the deep ocean (Hampton *et al.*, 1996; Nisbet & Piper, 1998; Pope *et al.*, 2015) and they can greatly affect the seafloor morphology by producing slide scars (Williams, 2016). The asymmetry of submarine canyons (i.e. the difference of height and slope gradient of canyon flanks) has been suggested to be caused by regional tectonics (Micallef *et al.*, 2012), the deflection of turbidity currents (Cossu *et al.*, 2015), and the interaction of turbidity currents and contour currents (Miramontes *et al.*, 2020). In this work, the marked asymmetry in the middle reach of the Taiwan Canyon is first reported, together with the large difference recorded in terms of canyon levée height (up to 400 m), differences rarely documented in other regions. The repeated submarine landslides have eroded the north-eastern levée in the middle reach of Taiwan Canyon, resulting in the asymmetrical geometry of Taiwan Canyon in its middle reach. These results provide a new case study and explanation related to the controlling factors of asymmetry in submarine canyons.

CONCLUSIONS

High-resolution multibeam bathymetric and multichannel seismic data are used in this study

to investigate the development and geomorphology of the Taiwan Canyon. The main conclusions are as follows:

1 Seafloor bedforms include two fields of sediment waves (Fields 1 and 2) and a series of plunge pools identified within and around the Taiwan Canyon. A seamount is located in the south-west part of the Taiwan Canyon, resulting in changes in the orientation of the latter, from north-west/south-east to nearly west–east.

2 Marked asymmetry is observed in the middle reach of the Taiwan Canyon. The south-west bank of the canyon is much higher than its north-east counterpart, showing an average height difference of up to 400 m. The south-west bank of the canyon reveals more erosion than the opposite bank.

3 Recurrent slope failures sourced from the north-east side of the middle reach of the Taiwan Canyon are considered as the main reason for the obvious difference in canyon bank heights. Variations in the erosion power of landslides and turbidity currents are due to the effect of the inertial centrifugal forces.

4 Sediment waves in Field 1 are related to turbidity currents sourced from Branch 1 of the Taiwan Canyon. They are also associated with marked hydraulic jumps of *ca* 300 m. The velocity of turbidity currents flowing through the stoss and lee sides of sediment waves ranges from 2.16 to 3.31 m s^{-1} and 2.17 to 3.4 m s^{-1}, respectively.

5 Three sources of turbidity currents are proposed to be responsible for the formation of sediment waves in Field 2. The most likely scenario is that the turbidity currents overspill the Taiwan Canyon due to inertial centrifugal forces. Turbidity currents from Dongsha Channel and submarine canyons in the north of Taiwan Canyon might also contribute to the generation of sediment waves in Field 2.

6 Plunge pools are observed close to the northern bank of the Taiwan Canyon, and their formation is related to erosion imposed by turbidity currents sourced from the submarine canyons in the north of Taiwan Canyon. The northern banks of plunge pools reveal steeper slope gradients than their opposite sides.

ACKNOWLEDGEMENTS

This work was financially supported by Guangdong Basic and Applied Basic Research Foundation (2020B1515020016), Key Special Project for Introduced Talents Team of Southern Marine Science and Engineering Guangdong Laboratory (Guangzhou) (GML2019ZD0104), National Natural Science Foundation of China (41706054 and 41876054) and National Natural Science Foundation of Guangdong Province (2020A1515010497). Dr Wei Li is funded by the CAS Pioneer Hundred Talents Program. The editors (Dr Ian Kane and Prof. Dr Zhifei Liu), Dr Chenglin Gong and two anonymous reviewers are thanked for their constructive comments.

NOMENCLATURE

F_i	Internal Froude number of turbidity currents
C_f	Drag coefficient at the seafloor
e	Entrainment coefficient
h	Flow thickness
L	Wavelength of sediment waves
u	Velocity of turbidity currents flowing sediment waves
C	Volume concentration
g	Gravitational acceleration
α	Slope gradient of sediment waves
$\Delta\rho$	(grain density – density of turbidity currents)/seawater density
Fr_1	Froude number before hydraulic jumps
Fr	Froude number after hydraulic jumps

DATA AVAILABILITY STATEMENT

The data that support the findings of this study are available from the corresponding author upon reasonable request.

REFERENCES

Aarseth, I., **Lønne, Ø.** and **Giskeødegaard, O.** (1989) Submarine slides in glaciomarine sediments in some western Norwegian fjords. *Marine Geology*, **88**, 1–21.

Arzola, R.G., **Wynn, R.B.**, **Lastras, G.**, **Masson, D.G.** and **Weaver, P.P.E.** (2008) Sedimentary features and processes in the Nazaré and Setúbal submarine canyons, west Iberian margin. *Mar. Geol.*, **250**, 64–88.

Betzler, C., **Lindhorst, S.**, **Eberli, G.P.**, **Lüdmann, T.**, **Möbius, J.**, **Ludwig, J.**, **Schutter, I.**, **Wunsch, M.**, **Reijmer, J.J.G.** and **Hübscher, C.** (2014) Periplatform drift: The combined

result of contour current and off-bank transport along carbonate platforms. *Geology*, **42**, 871–874.

Bowen, A.J., **Normark, W.R.** and **Piper, D.J.W.** (1984) Modelling of turbidity currents on Navy Submarine Fan, California Continental Borderland. *Sedimentology*, **31**, 169–185.

Canals, M., **Puig, P.**, **de Madron, X.D.**, **Heussner, S.**, **Palanques, A.** and **Fabres, J.** (2006) Flushing submarine canyons. *Nature*, **444**, 354–357.

Casalbore, D., **Clare, M.A.**, **Pope, E.L.**, **Quartau, R.**, **Bosman, A.**, **Chiocci, F.L.**, **Romagnoli, C.** and **Santos, R.** (2020) Bedforms on the submarine flanks of insular volcanoes: New insights gained from high resolution seafloor surveys. *Sedimentology*. https://doi.org/10.1111/sed.12725

Clague, D.A. and **Moore, J.G.** (2002) The proximal part of the giant submarine Wailau landslide, Molokai. *Hawaii. Journal of Volcanology and Geothermal Research*, **113**, 259–287.

Cossu, R., **Wells, M.G.** and **Wåhlin, A.K.** (2010) Influence of the Coriolis force on the velocity structure of gravity currents in straight submarine channel systems. *J. Geophys. Res.*, **115**. https://doi.org/10.1029/2010JC006208

Cossu, R. and **Wells, M.G.** (2013) The evolution of submarine channels under the influence of Coriolis forces: experimental observations of flow structures. *Terra Nova*, **25**, 65–71.

Cossu, R., **Wells, M.G.** and **Peakall, J.** (2015) Latitudinal variations in submarine channel sedimentation patterns: the role of Coriolis forces. *J. Geol. Soc.*, **172**, 161–174.

Covault, J.A., **Kostic, S.**, **Paull, C.K.**, **Ryan, H.F.** and **Fildani, A.** (2014) Submarine channel initiation, filling and maintenance from sea-floor geomorphology and morphodynamic modelling of cyclic steps. *Sedimentology*, **61**, 1031–1054.

Dantec, N.L., **Hogarth, L.J.**, **Driscoll, N.W.**, **Babcock, J.M.**, **Barnhardt, W.A.** and **Schwab, W.C.** (2010) Tectonic controls on nearshore sediment accumulation and submarine canyon morphology offshore La Jolla, Southern California. *Mar. Geol.*, **268**, 115–128.

Ding, W., **Li, J.B.**, **Han, X.Q.**, **Suess, E.**, **Huang, Y.Y.**, **Qiu, X.L.** and **Li, M.B.** (2010) Morphotectonics and formation of the Taiwan Bank Canyon, southwest offshore Taiwan Island. *J. Oceanogr. Marine Sci.*, **14**, 65–78.

Ding, W.W., **Li, J.B.**, **Li, J.**, **Fang, Y.X.** and **Tang, Y.** (2013) Morphotectonics and evolutionary controls on the Pearl River Canyon system, South China Sea. *Mar. Geophys. Res.*, **34**, 221–238.

Fildani, A., **Normark, W.R.**, **Kostic, S.** and **Parker, G.** (2006) Channel formation by flow stripping: Large-scale scour features along the Monterey East Channel and their relation to sediment waves. *Sedimentology*, **53**, 1265–1287.

Fonnesu, M., **Palermo, D.**, **Galbiati, M.**, **Marchesini, M.**, **Bonamini, E.** and **Bendias, D.** (2020) A new world-class deep-water play-type, deposited by the syndepositional interaction of turbidity flows and bottom currents: The giant Eocene Coral Field in northern Mozambique. *Mar. Pet. Geol.*, **111**, 179–201.

Gamberi, F., **Breda, A.** and **Mellere, D.** (2017) Depositional canyon heads at the edge of narrow and tectonically steepened continental shelves: comparing geomorphic elements, processes and facies in modern and outcrop examples. *Marine and Petroleum Geology*, **87**, 157–170.

Gong, C.L., **Wang, Y.M.**, **Zhu, W.L.**, **Li, W.G.**, **Xu, Q.** and **Zhang, J.M.** (2011) The Central Submarine Canyon in the Qiongdongnan Basin, northwestern South China Sea: architecture, sequence stratigraphy, and depositional processes. *Mar. Pet. Geol.*, **28**, 1690–1702.

Gong, C.L., **Wang, Y.M.**, **Peng, X.C.**, **Li, W.G.**, **Qiu, Y.** and **Xu, S.** (2012) Sediment waves on the South China Sea Slope off southwestern Taiwan: implications for the intrusion of the Northern Pacific Deep Water into the South China Sea. *Mar. Pet. Geol.*, **32**, 95–109.

Gong, C.L., **Wang, Y.M.**, **Zhu, W.L.**, **Li, W.G.** and **Xu, Q.** (2013) Upper Miocene to Quaternary unidirectionally migrating deep-water channels in the Pearl River mouth Basin, northern South China Sea. *AAPG Bulletin*, **97**, 285–308.

Gong, C.L., **Wang, Y.M.**, **Xu, S.**, **Pickering, K.T.**, **Peng, X.C.**, **Li, W.G.** and **Yan, Q.** (2015) The northeastern South China Sea margin created by the combined action of down-slope and along-slope processes: Processes, products and implications for exploration and paleoceanography. *Mar. Pet. Geol.*, **64**, 233–249.

Gong, C.L., **Wang, Y.M.**, **Rebesco, M.**, **Salon, S.** and **Steel, R.J.** (2018) How do turbidity flows interact with contour currents in unidirectionally migrating deep-water channels? *Geology*, **46**, 551–554.

Hampton, M.A., **Lee, H.J.** and **Locat, J.** (1996) Submarine landslides. *Rev. Geophys.*, **34**(1), 33–59.

Harris, P.T., **Barrie, J.V.**, **Conway, K.W.** and **Greene, H.G.** (2014) Hanging canyons of Haida Gwaii, British Columbia, Canada: faultcontrol on submarine canyon geomorphology along active continental margins. *Deep Sea Research Part II: Topical Studies in Oceanography*, **104**, 83–92.

He, Y., **Zhong, G.F.**, **Wang, L.L.** and **Kuang, Z.G.** (2014) Characteristics and occurrence of submarine canyon-associated landslides in the middle of the northern continental slope, South China Sea. *Mar. Pet. Geol.*, **57**, 546–560.

Heap, A. and **Harris, P.** (2008) Geomorphology of the Australian margin and adjacent seafloor. *Aust. J. Earth. Sci.*, **55**, 555–585.

Hill, P., **Moran, K.** and **Blasco, S.** (1982) Creep deformation of slope sediments in the Canadian Beaufort Sea. *Geo-Mar. Lett.*, **2**, 163.

Hsu, S.K., **Yeh, Y.C.**, **Doo, W.B.** and **Tsai, C.H.** (2004) New bathymetry and magnetic lineations identifications in the northernmost South China Sea and their tectonic implications. *Mar. Geophys. Res.*, **25**, 29–44.

Keevil, G.M., **Peakall, J.** and **Best, J.L.** (2007) The influence of scale, slope and channel geometry on the flow dynamics of submarine channels. *Mar. Pet. Geol.*, **24**, 487–503.

Kostic, S. (2014) Upper flow regime bedforms on levées and continental slopes, Turbidity current flow dynamics in response to fine-grained sediment waves. *Geosphere*, **10**, 1094–1103.

Kuang, Z.G., **Zhong, G.F.**, **Wang, L.L.** and **Guo, Y.Q.** (2014) Channel-related sediment waves on the eastern slope offshore Dongsha Islands, northern South China Sea. *J. Asian. Earth. Sci.*, **79**, 540–551.

Lamb, M.P., **Parsons, J.D.**, **Mullenbach, B.L.**, **Finlayson, D.P.**, **Orange, D.L.** and **Nittrouer, C.A.** (2008) Evidence for superelevation, channel incision, and formation of cyclic steps by turbidity currents in Eel Canyon, California. *Geol. Soc. Am. Bull.*, **120**, 463–475.

Lee, S.E., **Talling, P.J.**, **Ernst, G.G.** and **Hogg, A.J.** (2002) Occurrence and origin of submarine plunge pools at the base of the US continental slope. *Mar. Geol.*, **185**, 363–377.

Lee, S.H. and **Chough, S.K.** (2001) High-resolution (2–7 kHz) acoustic and geometric characters of submarine creep

deposits in the South Korea Plateau, East Sea. *Sedimentology*, **48**, 629–644.

Li, X.Q., **Fairweather, L.**, **Wu, S.G.**, **Ren, J.Y.**, **Zhang, H.J.**, **Quan, X.Y.**, **Jiang, T.**, **Zhang, C.**, **Su, M.**, **He, Y.L.** and **Wang, D.W.** (2013) Morphology, sedimentary features and evolution of a large palaeo submarine canyon in Qiongdongnan basin, Northern South China Sea. *J. Asian Earth Sci.*, **62**, 685–696.

Liao, W.Z., **Lin, A.T.**, **Liu, C.S.**, **Oung, J.N.** and **Wang, Y.** (2016) A study on tectonic and sedimentary development in the rifted northern continental margin of the South China Sea near Taiwan. *Interpretation.*, **4**, 47–65.

Liu, J.T., **Kao, S.J.**, **Huh, C.A.** and **Hung, C.C.** (2013) Gravity flows associated with flood events and carbon burial: Taiwan as instructional source area. *Annu. Rev. Mar. Sci.*, **5**, 47–68.

Liu, Z.F., **Zhao, Y.L.**, **Colin, C.**, **Stattegger, K.**, **Wiesner, M.G.**, **Huh, C.A.**, **Zhang, Y.W.**, **Li, X.**, **Sompongchaiyakul, P.** and **You, C.F.** (2016) Source-to-sink transport processes of fluvial sediments in the South China Sea. *Earth Sci. Rev.*, **153**, 238–273.

Masson, D., **Howe, J.** and **Stoker, M.** (2002) Bottom-current sediment waves, sediment drifts and contourites in the northern Rockall Trough. *Mar. Geol.*, **192**, 215–237.

Meiburg, E. and **Kneller, B.** (2010) Turbidity currents and their deposits. *Annu. Rev. Fluid. Mech.*, **42**, 135–156.

Micallef, A., **Mountjoy, J.J.**, **Canals, M.** and **Lastras, G.** (2012) Deep-seated bedrock landslides and submarine canyon evolution in an active tectonic margin: Cook Strait, New Zealand. In: *Submarine Mass Movements and their Consequences* (Ed. Yamada, Y.) Vol. **31**, pp. 201–212. Springer, Dordrecht. https://link.springer.com/chapter/10.1007/978-94-007-2162-3_18

Micallef, A., **Mountjoy, J.J.**, **Barnes, P.M.**, **Canals, M.** and **Lastras, G.** (2014) Geomorphic response of submarine canyons to tectonic activity: Insights from the Cook Strait canyon system, New Zealand. *Geosphere*, **10**, 905–929.

Miramontes, E., **Eggenhuisen, J.T.**, **Jacinto, R.S.**, **Poneti, G.**, **Pohl, F.**, **Normandeau, A.**, **CampbellF, D.C.** and **Javier Hernández-Molina, F.** (2020) Channel-levee evolution in combined contour current–turbidity current flows from flume-tank experiments. *Geology*, **48**(4), 353–357.

Mountjoy, J.J., **Barnes, P.M.** and **Pettinga, J.R.** (2009) Morphostructure and evolution of submarine canyons across an active margin: Cook Strait sector of the Hikurangi Margin, New Zealand. *Mar. Geol.*, **260**, 45–68.

Nisbet, E.G. and **Piper, D.J.** (1998) Giant submarine landslides. *Nature*, **392**, 329–330.

Normandeau, A., **Campbell, D.C.** and **Cartigny, M.J.B.** (2018) The influence of turbidity currents and contour currents on the distribution of deep-water sediment waves offshore eastern Canada. *Sedimentology*, **66**, 1746–1767.

Normark, W.R., **Piper, D.J.**, **Posamentier, H.**, **Pirmez, C.** and **Migeon, S.** (2002) Variability in form and growth of sediment waves on turbidite channel levees. *Mar. Geol.*, **192**, 23–58.

Paull, C.K., **Caress, D.W.**, **Ussler, W.**, **Lundsten, E.** and **Meiner-Johnson, M.** (2011) High-resolution bathymetry of the axial channels within Monterey and Soquel submarine canyons, offshore central California. *Geosphere*, **7**, 1077–1101.

Paull, C.K., **Talling, P.J.**, **Maier, K.L.**, **Parsons, D.**, **Xu, J.P.**, **Caress, D.W.**, **Gwiazda, R.**, **Lundsten, E.M.**, **Anderson, K.** and **Barry, J.P.** (2018) Powerful turbidity currents driven by dense basal layers. *Nat. Commun.*, **9**, 1–9.

Piper, D.J.W. and **Savoye, B.** (1993) Processes of late Quaternary turbidity current flow and deposition on the Var deep-sea fan, north-west Mediterranean Sea. *Sedimentology*, **40**, 557–582.

Pope, E., **Talling, P.J.**, **Urlaub, M.**, **Hunt, J.**, **Clare, M.** and **Challenor, P.** (2015) Are large submarine landslides temporally random or do uncertainties in available age constraints make it impossible to tell? *Mar. Geol.*, **369**, 19–33.

Pope, E.L., **Jutzeler, M.**, **Cartigny, M.J.B.**, **Shreeve, J.**, **Talling, P.J.**, **Wright, I.C.** and **Wysoczanski, R.J.** (2018) Origin of spectacular fields of submarine sediment waves around volcanic islands. *Earth Planet Sci. Lett.*, **493**, 12–24.

Pratson, L.F. and **Coakley, B.J.** (1996) A model for the headward erosion of submarine canyons induced by downslope-eroding sediment flows. *Geol. Soc. Am. Bull.*, **108**, 225–234.

Schnyder, J.S.D., **Eberli, G.P.**, **Betzler, C.**, **Wunsch, M.**, **Lindhorst, S.**, **Schiebel, L.**, **Mulder, T.** and **Ducassou, E.** (2018) Morphometric analysis of plunge pools and sediment wave fields along western Great Bahama Bank. *Mar. Geol.*, **397**, 15–28.

Sibuet, J.C., **Hsu, S.K.**, **Le Pichon, X.**, **Le Formal, J.P.**, **Reed, D.**, **Moore, G.** and **Liu, C.S.** (2002) East Asia plate tectonics since 15 Ma: constraints from the Taiwan region. *Tectonophysics*, **344**, 103–134.

Stow, D.A., **Faugères, J.C.**, **Viana, A.** and **Gonthier, E.** (1998) Fossil contourites, a critical review. *Sed. Geol.*, **115**, 3–31.

Symons, W.O., **Sumner, E.J.**, **Talling, P.J.**, **Cartigny, M.J.** and **Clare, M.A.** (2016) Large-scale sediment waves and scours on the modern seafloor and their implications for the prevalence of supercritical flows. *Mar. Geol.*, **371**, 130–148.

Talling, P.J., **Wynn, R.B.**, **Masson, D.G.**, **Frenz, M.**, **Cronin, B.T.**, **Schiebel, R.**, **Akhmetzhanov, A.M.**, **Dallmeier-Tiessen, S.**, **Benetti, S.**, **Weaver, P.P.E.**, **Georgiopoulou, A.**, **Zühlsdorff, C.** and **Amy, L.A.** (2007) Onset of submarine debris flow deposition far from original giant landslide. *Nature*, **450**, 541–544.

Talling, P.J., **Masson, D.G.**, **Sumner, E.J.** and **Malgesini, G.** (2012) Subaqueous sediment density flows: Depositional processes and deposit types. *Sedimentology*, **59**, 1937–2003.

Taylor, B. and **Hayes, D.E.** (1983) Origin and history of the South China Sea basin. *Tectonic. Geologic. Evol. Southeast Asian Seas Islands: Part 2*, **27**, 23–56.

Wang, T.K., **Chen, M.K.**, **Lee, C.S.** and **Xia, K.Y.** (2006) Seismic imaging of the transitional crust across the northeastern margin of the South China Sea. *Tectonophysics*, **412**, 237–254.

Wang, K.L., **Lo, Y.M.**, **Chung, S.L.**, **Lo, C.H.**, **Hsu, S.K.**, **Yang, H.J.** and **Shinjo, R.** (2012) Age and Geochemical Features of Dredged Basalts from Offshore SW Taiwan: The Coincidence of Intra-Plate Magmatism with the Spreading South China Sea. *Terrest. Atmos. Ocean Sci.*, **23**(6), 657.

Wang, X.X., **Wang, Y.M.**, **He, M.**, **Chen, W.T.**, **Zhuo, H.T.**, **Gao, S.M.**, **Wang, M.H.** and **Zhou, J.W.** (2017) Genesis and evolution of the mass transport deposits in the middle segment of the Pearl River canyon, South China Sea: Insights from 3D seismic data. *Mar. Pet. Geol.*, **88**, 555–574.

Williams, S.C.P. (2016) News Feature: Skimming the surface of underwater landslides. *Proc. Natl. Acad. Sci.*, **113**, 1675–1678.

Wynn, R.B., **Weaver, P.P.**, **Ercilla, G.**, **Stow, D.A.** and **Masson, D.G.** (2000) Sedimentary processes in the Selvage

sediment-wave field, NE Atlantic: new insights into the formation of sediment waves by turbidity currents. *Sedimentology*, **47**, 1181–1197.

Wynn, R.B. and **Stow, D.A.** (2002) Classification and characterisation of deep-water sediment waves. *Mar. Geol.*, **192**, 7–22.

Xu, S., **Wang, Y.M.**, **Peng, X.C.**, **Zou, H.Y.**, **Qiu, Y.**, **Gong, C.L.** and **Zhuo, H.T.** (2014) Origin of Taiwan Canyon and its effects on deepwater sediment. *Sci. China Earth Sci.*, **57**, 2769–2780.

Yeh, Y.C., **Sibuet, J.C.**, **Hsu, S.K.** and **Liu, C.S.** (2010) Tectonic evolution of the Northeastern South China Sea from seismic interpretation. *J. Geophys. Res.*, **115**. https://doi.org/10.1029/2009JB006354

Yin, S.R., **Wang, L.L.**, **Guo, Y.Q.** and **Zhong, G.F.** (2015) Morphology, sedimentary characteristics, and origin of the Dongsha submarine canyon in the northeastern continental slope of the South China Sea. *Sci.China Earth Sci.*, **58**, 971–985.

Yin, S.R., **Lin, L.**, **Pope, E.L.**, **Li, J.B.**, **Ding, W.F.**, **Wu, Z.**, **Ding, W.W.**, **Gao, J.** and **Zhao, D.N.** (2019) Continental slope-confined canyons in the Pearl River Mouth Basin in the South China Sea dominated by erosion, 2004–2018. *Geomorphology*, **344**, 60–74.

Zhang, Y.W., **Liu, Z.F.**, **Zhao, Y.L.**, **Colin, C.**, **Zhang, X.D.**, **Wang, M.**, **Zhao, S.H.** and **Kneller, B.** (2018) Long-term in situ observations on typhoon-triggered turbidity currents in the deep sea. *Geology*, **46**, 675–678.

Zhao, F., **Alves, T.M.**, **Wu, S.G.**, **Li, W.**, **Huuse, M.**, **Mi, L.J.**, **Sun, Q.L.** and **Ma, B.J.** (2016) Prolonged post-rift magmatism on highly extended crust of divergent continental margins (Baiyun Sag, South China Sea). *Earth Planet Sci. Lett.*, **445**, 79–91.

Zhong, G.F., **Cartigny, M.J.**, **Kuang, Z.G.** and **Wang, L.L.** (2015) Cyclic steps along the South Taiwan Shoal and West Penghu submarine canyons on the northeastern continental slope of the South China Sea. *Geol. Soc. Am. Bulletin.*, **127**, 804–824.

Manuscript received 3 February 2020; revision 10 October 2020; revision accepted 16 October 2020